Plasmonics (2024) 19:2729–2742
https://doi.org/10.1007/s11468-024-02194-8

RESEARCH

ARF Dual-Channel Magnetic Field and Temperature Sensor Based on the SPR Effect

Meiqi Liu[1] · Xianli Li[1] · Wei Liu[1] · Xili Lu[2] · Jingwei Lv[1] · Kong Xiangzhuo[3] · Lin Yang[1] · Jianxin Wang[1] · Paul K. Chu[4] · Chao Liu[1]

Received: 8 December 2023 / Accepted: 4 January 2024 / Published online: 24 January 2024

Abstract

An anti-resonant fiber (ARF) surface plasmon resonance (SPR) dual-parameter sensor is designed for simultaneous detection of the magnetic field and temperature. Both sides of the fiber core in the sensor are filled with gold nanowires and gold dielectrics, respectively, to excite SPR. The center air hole in the ARF is filled with a magnetic fluid (MF) which responds to the magnetic field and temperature, and the temperature measurement is carried out by putting polydimethylsiloxane (PDMS) outside the gold nanowires. Analysis by the finite element method reveals maximum first and second resonance peak sensitivities of 300 pm/Oe and 500 pm/Oe, respectively, when the magnetic field is between 50 and 130 Oe. The maximum wavelength sensitivity of the second resonance peak is 10.8 nm/°C in the temperature range of 20–30 °C. Temperature cross-sensitization due to the magnetohydrothermo-optical effects is overcome by building and demodulating the sensing matrix. This new sensor design is very promising in fields such as industrial automation, military application, and geological exploration.

Keywords Anti-resonant fiber · Surface plasmon resonance · Sensing · Magnetic field · Temperature · Dual-parameter sensing

Introduction

Magnetic field sensors such as magnetostrictive sensors, hall effect devices, magnetoresistive sensors, and magnetic induction sensors are widely used in industrial automation, automotive electronics, and smartphones [1–3]. However, these traditional sensors have some disadvantages such as the need for additional temperature control systems, high cost, high power consumption, and poor remote monitoring capabilities [4, 5]. In this respect, optical fiber magnetic field sensors with a small size, fast response, low cost, and high interference immunity have been developed [6]. For example, Yang et al. have proposed to use magnetostrictive TbDyFe thin films as the magnetic sensing materials in optical fibers. The TbDyFe thin films are deposited on the etched side circles of the fiber Bragg grating (FBG) by magnetron sputtering to accomplish both magnetic and current sensing [7]. Paliwal et al. have applied the SPR technique to study the optical properties of Ce- and Mn-doped $BiFeO_3$ thin films. The dependence of the magnetic field on the optical properties of the doped $BiFeO_3$ films is determined by utilizing pulsed laser deposition of $BiFeO_3$ films and SPR [8]. However, these sensors have some drawbacks because the film thickness and location are difficult to control and production is quite complicated and costly.

Nanomaterial magnetofluids have spurred the development of optical fiber magnetic field sensors due to their multiple magneto-optical properties such as tunable refractive index (RI) [9], magnetic volume change [10], and magnetic dielectric anisotropy [11]. By means of encapsulation, the liquid state of the magnetic fluid (MF) can bond easily with the fiber compared with the coating process [12]. Several

✉ Xianli Li
lxl7158@163.com

✉ Chao Liu
msm-liu@126.com

1 School of Physics and Electronic Engineering, Northeast Petroleum University, Daqing 163318, People's Republic of China

2 School of Materials Science and Chemical Engineering, Harbin Engineering University, Harbin 150001, China

3 School of Foreign Languages, Civil Aviation University of China, Tianjin 300300, China

4 Department of Physics, Department of Materials Science and Engineering, and Department of Biomedical Engineering, City University of Hong Kong, Tat Chee Avenue, Kowloon, Hong Kong, China

types of optical fiber magnetic field sensors based on MF have been proposed, for instance, photonic crystal fiber [13], Fabry-Perot fiber [14], single mode-multimode-single mode fiber fusion splicing [15], anti resonant fiber (ARF) [16], and so on. However, the detection of individual physical parameters is still inaccurate due to cross-sensitivity issues, and consequently, multiparameter sensors based on matrix demodulation have been proposed. Liu et al. have designed a temperature-compensated magnetic field sensor based on the coupling of surface plasmon resonance and directional resonance in a D-shape photonic crystal fiber and deduced the relationship between the resonance wavelength and applied magnetic field with a high sensitivity of 0.87 nm/mT [17]. K. A. et al. have proposed a highly sensitive magneto-fluidic (ethanol) temperature sensor based on a ring-core microstructured optical fiber (MOF) showing a magnetic field sensitivity of about 25,641.025 nm/RIU and temperature sensitivity of about 10 nm/°C in the ranges of 50–200 Oe and 10–60 °C [18]. Wang et al. have described a two-parameter sensor based on the surface plasmon resonance (SPR) photonic crystal fiber (PCF) for magnetic field and temperature detection. The magnetic field sensitivities of channel 1 and channel 2 are 65 pm/Oe and 0 pm/Oe, respectively, in the magnetic field range of 50–130 Oe and the temperature sensitivities of channel 1 and channel 2 are 520 pm/°C and 2360 pm/°C, respectively, in the range of 17.5–27.5 °C [19].

Although these aforementioned sensors offer certain advantages and improvements, one of the obvious drawbacks is the complex manufacturing process. In this respect, the anti-resonant fiber magnetic field sensor is simpler because it consists of a negative curvature anti-resonant tube with a certain thickness instead of the photonic crystal fiber with complex air holes. The photoconductive mechanism depends on suppressed coupling and anti-resonance conditions between modes in the core and cladding [20, 21]. Compared with previously reported single-parameter sensors, our proposed structure consisting of 10 sets of negative curvature tubes provides a rich design dimension for multiparameter measurements, effectively improves the performance of the ARF-SPR sensor and solves the temperature-induced cross-sensitization problem.

Herein, a novel ARF-SPR dual-channel magnetic field temperature sensor comprising 10 sets of conjoined tubes is designed for simultaneous detection of the magnetic field and temperature. The surface plasma waves (SPW) are excited by placing gold nanowires and gold dielectrics on both sides of the fiber core. The temperature-sensitive PDMS is put outside the gold nanowires, and the fiber core is filled with the magnetic field-sensitive MF. The magnetic field and temperature are measured by detecting the displacement of the coupled waves. To optimize the structure and performance, the mode coupling, resolution, structural parameter sensitivity, linearity, and other characteristics of the sensor are analyzed and simulated by the COMSOL software. The results indicate that the sensor can accurately detect magnetic field and temperature in the ranges of 50–130 Oe and 20–30 °C, respectively. The parameters of the sensor are optimized based on the wavelength sensitivities at magnetic fields between 50 and 70 Oe and temperature between 20 and 22.5 °C. In the magnetic field range of 50–130 Oe, the average sensitivities of the first resonance peak and the second resonance peak are 237.5 pm/Oe and 400 pm/Oe with minimum resolutions of 0.33 Oe and 0.2 Oe, respectively. The average wavelength sensitivity of the second resonance peak is 10.6 nm/°C with a minimum resolution of 0.0096 °C in the temperature range of 20–30 °C. This sensor design overcomes the problem of cross-sensitivity due to the temperature variation by building and demodulating the sensing matrix boding well for application to navigation, smart devices, and smart grids [22].

ARF Design and Theory

The ARF-SPR-based two-parameter sensor is analyzed by COMSOL software. The cross-section and 3D cross-section of the sensor are depicted in Fig. 1a and b.

The structural parameters, Λ, d_1, d_2, d_3, t, R_1, R_2, and R_3, are represented as the distance from the central stomata to the center of the inner tube, inner tube diameter, outer tube diameter, diameter of the gold nanowire, the thickness of the tube wall, radius of the cladding layer, and radius of the perfectly matched layer, respectively. The initial parameters of the anti-resonant fiber (ARF) are as follows: $\Lambda = 9.6$ μm, $d_1 = 2*(\Lambda*\sin(0.1*\Pi))-2*t$, $d_2 = 6$ μm, $d_3 = 1$ μm, and $t = 0.5$ μm. The ARF consists of 10 sets of conjoined negative curvature tubes with the inner tubes being tangent to form the fiber core for light transmission. The glass tube on the left side of the fiber core is filled with gold nanowires, and the glass tube on the right side is filled directly with gold dielectrics, thus generating two resonance peaks for bidirectional sensing of temperature and magnetic field. The glass tube to the left of the fiber core is filled with a temperature-sensitive liquid (PDMS) in addition to gold nanowires [23]. Finally, the middle of the 10 sets of conjoined tubes are filled with a magnetic fluid (MF) [6]. The white area is air with a refractive index of 1. SiO_2 is a commonly used fiber material in optical fibers, with low cost, chemical and thermal stability, as well as controllable morphology and porosity [24–26]. We change the refractive indices of the core and cladding by doping SiO_2 with different elements to obtain the optimal fiber structure. Therefore, it is often chosen as background material. The blue region is the SiO_2 glass tube with a negative curvature, and the refractive index is calculated by the Sellmeier equation [27]:

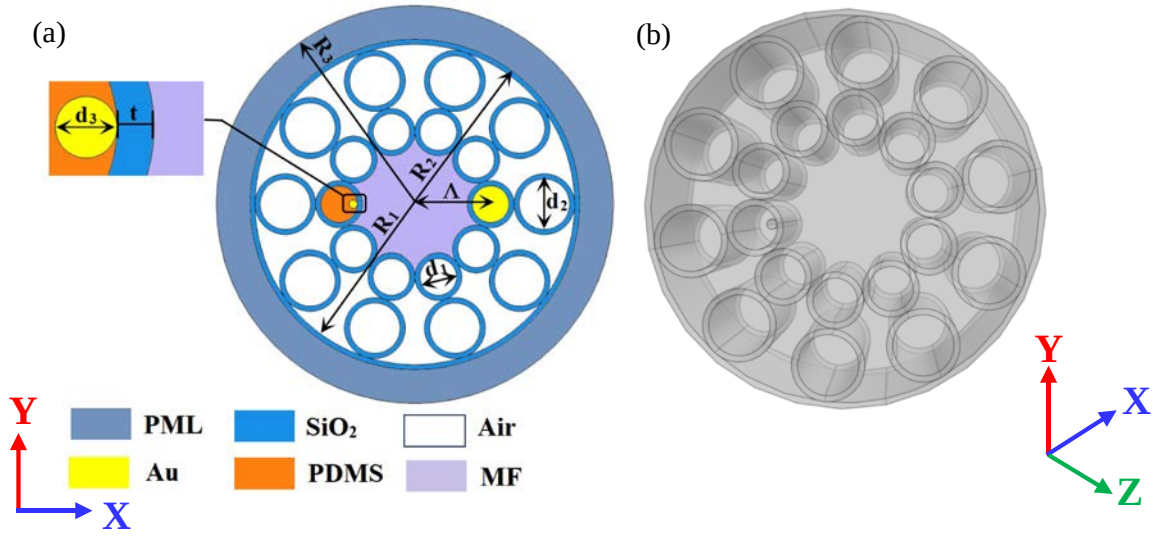

Fig. 1 **a** Cross-section and **b** 3D cross-section of the ARF-SPR sensor

$$n^2(\lambda) = 1 + \frac{A_1\lambda^2}{\lambda^2 - B_1} + \frac{A_2\lambda^2}{\lambda^2 - B_2} + \frac{A_3\lambda^2}{\lambda^2 - B_3}\,, \tag{1}$$

where $A_1 = 0.6961663$, $A_2 = 0.4079426$, $A_3 = 0.897479$, $B_1 = 0.0684043$, $B_2 = 0.1162414$, and $B_3 = 9.896161$. $n(\lambda)$ representing the refractive index of the medium, λ is the wavelength of light. A_i, B_i represent polarizations associated with specific optical properties of the material, and the choice of these polarizations is obtained from experimental measurements. The yellow area is filled with gold used to excite SPR. Although there is a temperature-dependent Drude model, the Drude-Lorentz model better describes the dielectric constant of gold in a modest temperature range. Hence, the dielectric constant of gold is expressed in terms of the Drude-Lorentz model as [28]:

$$\varepsilon_{Au}(\varepsilon) = \varepsilon_\infty - \frac{\omega_p^2}{\omega(\omega + i\omega_\tau)}\,, \tag{2}$$

where $\varepsilon_\infty = 9.75$, $\omega_p = 1.36 \times 1016$ rad/s, and $\omega_\tau = 1.45 \times 1014$ rad/s. $\varepsilon_{Au}(\varepsilon)$ represents the dielectric constant of gold in an electromagnetic field. ε_∞ represents the dielectric constant at high frequencies, which indicates the static dielectric constant of a dielectric independent of the frequency of the electromagnetic wave. ω represents the electromagnetic wave frequency. ω_τ represents the relaxation time or decay rate of the Lorentz term, which determines the width of the focal peak. ω_p represents the frequency of the Lorentz term, which indicates the position of the frequency peak on the frequency axis. The purple region is filled with a magnetic fluid (MF). Since the refractive index properties are often used for optical sensing, it is necessary to introduce the refractive index as a function of the applied magnetic field, and the refractive index n_{MF} can be expressed as [29]:

$$n_{MF} = (n_2 - n_1)\left[\coth\left(\alpha\frac{H - H_0}{T}\right) - \frac{T}{\alpha(H - H_0)}\right] + n_1\,, \tag{3}$$

where n_2 is the saturation of the refractive index of the MF, n_1 is the initial refractive index of the MF, α is the fitting coefficient, T is the working temperature, H_0 is the threshold value of the magnetic field, and H is the external magnetic field intensity. Here, these parameters are set to $\alpha = 5$, $H_0 = 30$ Oe, $n_1 = 1.4352$, and $n_2 = 1.4385$. The orange region is filled with temperature-sensitive liquid (PDMS), a new temperature-sensitive substance with refractive indexes varying with temperature as shown by the following Eq. (4) [30].

$$n_{PDMS} = -4.5 \times 10^{-4}T + 1.4176\,, \tag{4}$$

where T represents the ambient temperature in ℃. The operating band of an anti-resonant fiber is determined by the anti-resonance conditions, and the selection of different glass tube thicknesses can lead to changes in the fiber operating bandwidth and loss characteristics. Accordingly, the glass tube thickness is one of the key parameters of the anti-resonant fiber as shown in Eq. (5) [31]:

$$t = \frac{\lambda m}{2 \times \sqrt{n_{glass}^2 - n_s^2}}\,, \tag{5}$$

where λ is the wavelength, m is the resonance order, and n_{glass} and n_s are the refractive indexes of SiO_2 and the analyte, respectively.

In order to improve the sensing characteristics, surface plasmon resonance (SPR) is exploited. The coupled model theory (CMT) can be used to analyze the SPR effect [32]. Figure 2 shows the basic principle of SPR, which represents the energy transfer between the fiber core and the metal surface. Electrons on the surface of the metal film move collectively in resonance at the metal-dielectric interface coupled with the incident light and propagate forward along the split interface to excite a surface plasma wave (SPW) that propagates along the surface of the metal film. When the two modes, that is, the SPP mode on the metal surface and the fundamental mode in the fiber core, satisfy the phase matching condition, most of the energy of the incident light will be converted into the SPW to stimulate SPR, consequently producing a sudden drop in the energy of the reflected light and resonant absorption peaks in the reflection spectrum. The change in the refractive index of the substance on the surface of the metal film can be determined by measuring the change in the specific wavelength corresponding to the resonance absorption peak. The refractive indexes of MF and PDMS change under the influence of the magnetic field and temperature. This allows the resonance wavelength corresponding to the SPR effect to change to realize magnetic field and temperature sensing. Materials with small thermo-optic coefficients contribute little to temperature sensing when the temperature varies over a small interval. Consequently, our work focuses on the effects of temperature on the refractive indexes of MF and PDMS, which have large thermo-optic coefficients.

The essence of SPR is the energy exchange between the fundamental mode and metal surface plasmon excitation (SPP) so that SPR can be monitored based on the loss spectrum of the fundamental mode. The loss of the fundamental mode at different wavelengths can be calculated by Eq. (6) [33]:

$$CL = \frac{2\pi}{\lambda}\frac{20}{\ln(10)}\mathrm{Im}\left(n_{\mathrm{eff}}\right)\Big/(\mathrm{dB/cm}), \tag{6}$$

where λ is the wavelength and $\mathrm{Im}(n_{\mathrm{eff}})$ is the imaginary part of the effective refractive index. SPR exists at a specific wavelength and changes regularly with the refractive index of the analyte. The structural parameters of the optical fiber have an important influence on the properties of the ARF-SPR sensor, and therefore, the wavelength sensitivity is monitored as an evaluation index to analyze the sensor. It is defined as the ratio of the difference in resonance wavelength (RW) of two neighboring analytes to the difference of the refractive indexes of two neighboring analytes as shown by Eq. (7) [34]:

$$S_{RW} = \frac{\Delta\lambda}{\Delta n}, \tag{7}$$

where $\Delta\lambda$ is the resonance wavelength change of the two-neighboring analytes and Δn is the refractive index difference between the two neighboring analytes. Here, we mainly investigate two-parameter sensing of the magnetic field and temperature and introduce the wavelength sensitivity for the temperature and magnetic field as shown by Eqs. (8) and (9):

$$S_{RW}(H) = \frac{\Delta\lambda_H}{\Delta H} \quad \text{and} \tag{8}$$

$$S_{RW}(T) = \frac{\Delta\lambda_T}{\Delta T}, \tag{9}$$

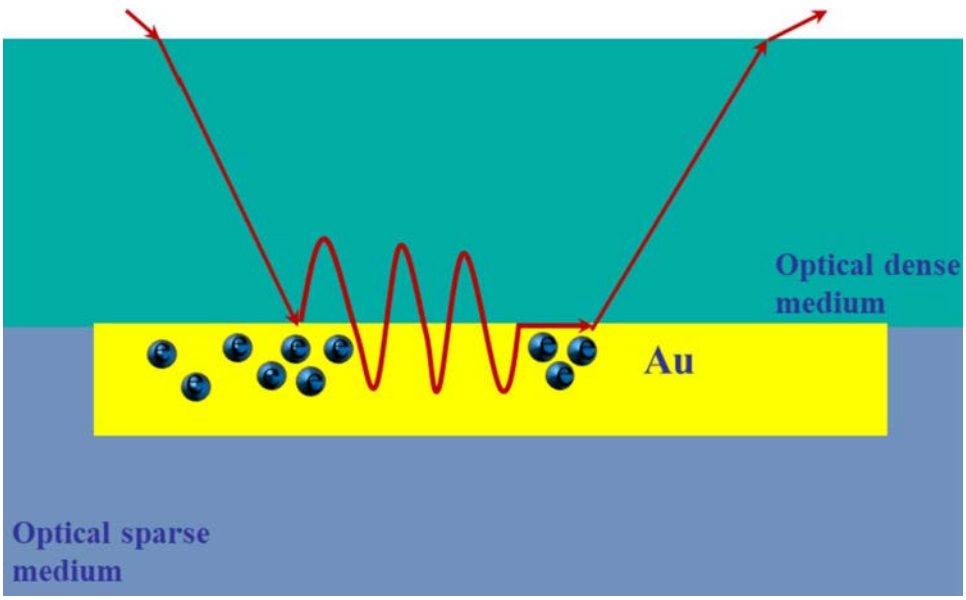

Fig. 2 Principle of SPR

where $\Delta\lambda_H$ is the resonant wavelength variation of the neighboring magnetic field and ΔH is the neighboring magnetic field variation, $\Delta\lambda_T$ is the resonance wavelength change for the adjacent temperature, and ΔT is the adjacent temperature change. In order to solve the cross-sensitivity problem caused by the magnetic field and temperature variations during sensing, a two-parameter sensitivity matrix is utilized to demodulate the magnetic field and temperature as shown by Eq. (10) [35]:

$$\begin{pmatrix} \Delta\lambda_1 \\ \Delta\lambda_2 \end{pmatrix} = \begin{pmatrix} S_{peak1}(H) & S_{peak1}(T) \\ S_{peak2}(H) & S_{peak2}(T) \end{pmatrix} \begin{pmatrix} \Delta H \\ \Delta T \end{pmatrix}, \tag{10}$$

where $\Delta\lambda_1$ and $\Delta\lambda_2$ denote the RW shifts of the two resonance peaks and $S_{peaki}(T)$ and $S_{paeki}(H)$ $(i=1,2)$ denote the temperature and magnetic field sensitivity of the first and second resonance peaks, respectively. The sensing matrices for the magnetic field and temperature can be obtained by back-calculating the sensitivity matrix by measuring the resonance wavelength shifts of the first resonance peak and the second resonance peak with changes in magnetic field and temperature, as shown by Eq. (11):

$$\begin{pmatrix} \Delta H \\ \Delta T \end{pmatrix} = \begin{pmatrix} S_{peak1}(H) & S_{peak1}(T) \\ S_{peak2}(H) & S_{peak2}(T) \end{pmatrix}^{-1} \begin{pmatrix} \Delta\lambda_1 \\ \Delta\lambda_2 \end{pmatrix}. \tag{11}$$

Based on the original parameters of the ARF described above, the mode characteristics of the sensor are analyzed at $T=20$ °C and $H=50$ Oe. Figure 3a and b present the loss spectra of the analyte in both polarization directions. It can be observed that y-pol exhibits only one resonance peak, while x-pol shows two resonance peaks, indicating that x-pol has more electric field components orthogonal to the gold nanowires and gold dielectrics. Actually, the x-pol characteristics are also observed to be superior to y-pol for the mode field distributions in Fig. 3a and b. The mode field variations before, during, and after the resonant coupling of SPR_{peak1} and SPR_{peak2} are depicted in Fig. 3(a), respectively. The energy in the fundamental mode is greater than in the SPP mode before resonant coupling. When the coupling point is reached, most of the energy in the fundamental mode is transferred to the SPP mode (i.e., SPR peak 1 fundamental mode energy is transferred to the SPP mode on the right side of the fundamental mode, and SPR peak 2 fundamental mode energy is transferred to the SPP mode on the left side of the fundamental mode). After coupling, the energy returns to the fundamental mode. The mode field distribution in Fig. 3b, on the other hand, cannot distinguish whether most of the energy of the fundamental mode is transferred into the left SPP mode or the right SPP mode for two-parameter sensing. Therefore, the x-pol model is chosen in our subsequent analysis.

The loss spectra generated by the x-pol modes and the real part of the effective refractive indexes of the x-pol fundamental and coupled SPP modes are shown in Fig. 4. The red, brown, and blue lines represent the effective refractive index real part of ($\mathrm{Re}(n_{eff})$) the fundamental mode, SPP mode 1 and SPP mode 2, respectively. The green line represent the fundamental mode CL associated with imaginary part of the effective refractive index $\mathrm{Im}(n_{eff})$. As the wavelength gradually increases, the $\mathrm{Re}(n_{eff})$ of the two modes decreases at different rates and the position of the SPP mode changes. At 1214 nm (SPP_{peak1}) and 1370 nm (SPP_{peak2}), SPP mode 1 and SPP mode 2 are coupled with the fundamental mode, respectively, and most of the energy of the fundamental mode is transferred into the SPP mode, which

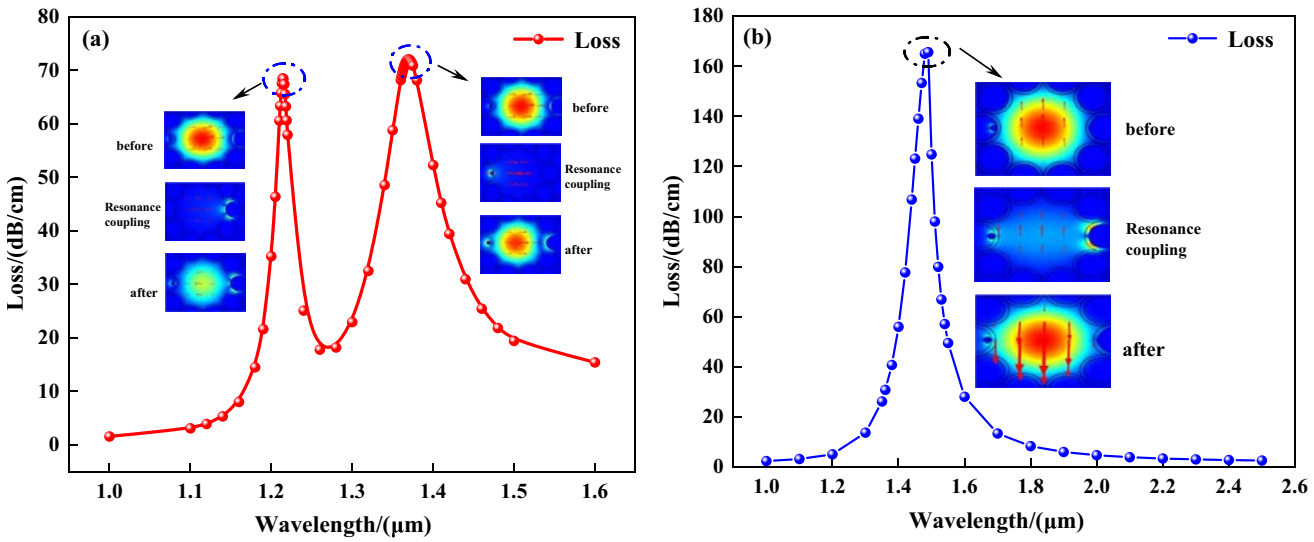

Fig. 3 Loss spectra of the x-pol core mode and y-pol core mode

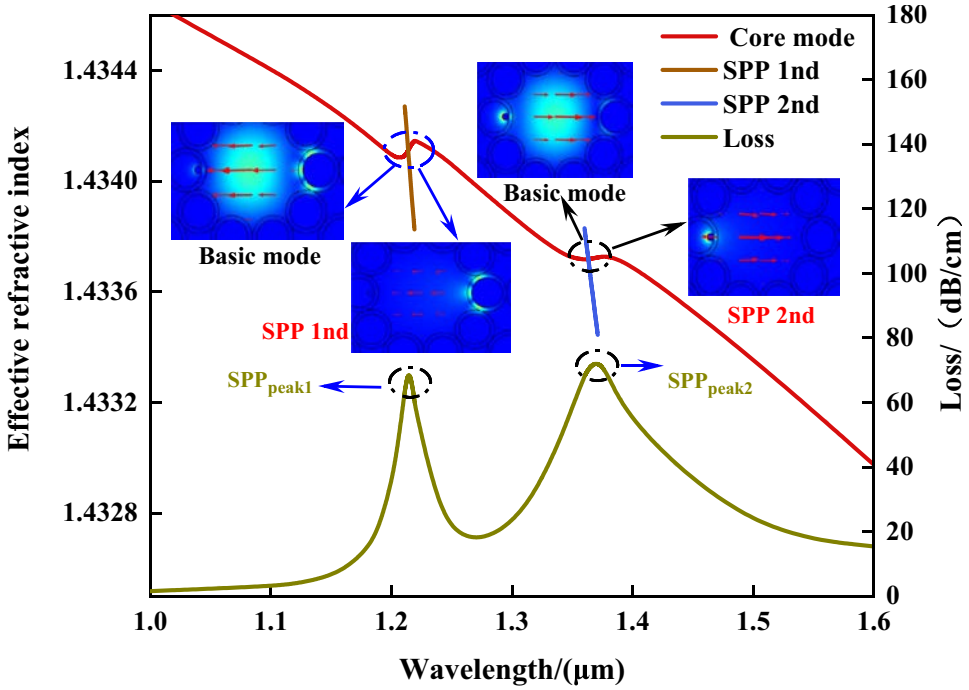

Fig. 4 Effective refractive indexes of the x-pol core mode and SPP modes and the loss spectrum of the ARF-SPR sensor

leads to a sudden decrease in the energy of the reflected light and produces two loss peaks at the intersection of the curves. This phenomenon satisfies the coupling theory. The results show that the curve trend is consistent with the energy coupling, and both modes satisfy the phase-matching condition to produce the SPR effect.

The finite element method (FEM) based on COMSOL software is utilized to study the sensing performance of the ARF-SPR sensor. When performing model construction, we usually build a circular perfect match layer in the outermost layer for reducing unnecessary electromagnetic reflections. It is worth mentioning that before the simulation, we also need to do a critical step of meshing this model to get more accurate results. To find a set of initial parameters suitable for structural optimization, a number of rough simulation calculations were performed to ensure the effective excitation of the SPR effect and the stable output of the sensor performance. In addition, when a large number of rough simulations are performed, the degree of influence of each parameter on the sensor performance is largely grasped, and the sensor performance is improved by further optimization.

Based on the degree of influence of parameters on sensor performance and structural characteristics, these important structural parameters are optimized in order from the inside out, which is gold line diameter d_3, inner tube diameter d_1, and tube wall thickness t. In addition, keeping other parameters unchanged while optimizing one parameter ensures both optimization and computational efficiency. The gold nanowire d_3 was first optimized using a single variable method. As shown in Fig. 1a, the outside of the gold nanowires is filled with a temperature-sensitive liquid, and so, the change in the structure of the gold nanowire may only play a role in the second resonance peak, which is confirmed by Fig. 5b. As d_3 increases, the first resonance peak resonant wavelength (RW) does not shift, while the second resonance peak shifts toward shorter wavelengths. To produce the optimal structure for practical fabrication, Fig. 5c shows the loss curves for different gold nanowire diameters at temperatures of 20 °C and 25 °C. The diameters of the gold nanowires are chosen to be in the range of 0.9–1.1 μm. As shown in Fig. 5d and e, the resonance intensity decreases gradually with increasing gold nanowire diameter. This is because the penetration depth of gold is only 20 to 30 nm, and when the diameter of the gold nanowires increases, the fiber core mode effectively shields the plasma excitations, leading to low coupling efficiency [36]. Figure 5f shows the curves of sensitivity versus loss for different d_3 at 20 °C. The wavelength sensitivity (WS) increases to 11 nm/°C with increasing d_3, but the loss is too small to efficiently excite SPR and the curve quality is poor. When $d_3 = 1$ μm, both loss and WS are at a moderate level and the curves are smoother. Consequently, the gold nanowire diameter d_3 is chosen to be 1 μm.

After determining the gold nanowire d_3, the effects of the inner tube d_1 on the sensing properties are determined as shown in Fig. 6b–f. It is shown to play a decisive role in the cladding constraint modal field. A d_1 that is too large cannot bind light to the fiber core thus limiting mode coupling, whereas a smaller d_1 leaves the modal field unconstrained leading to unstable beam transmission. According to the geometric relationship between d_1 and Λ, varying Λ

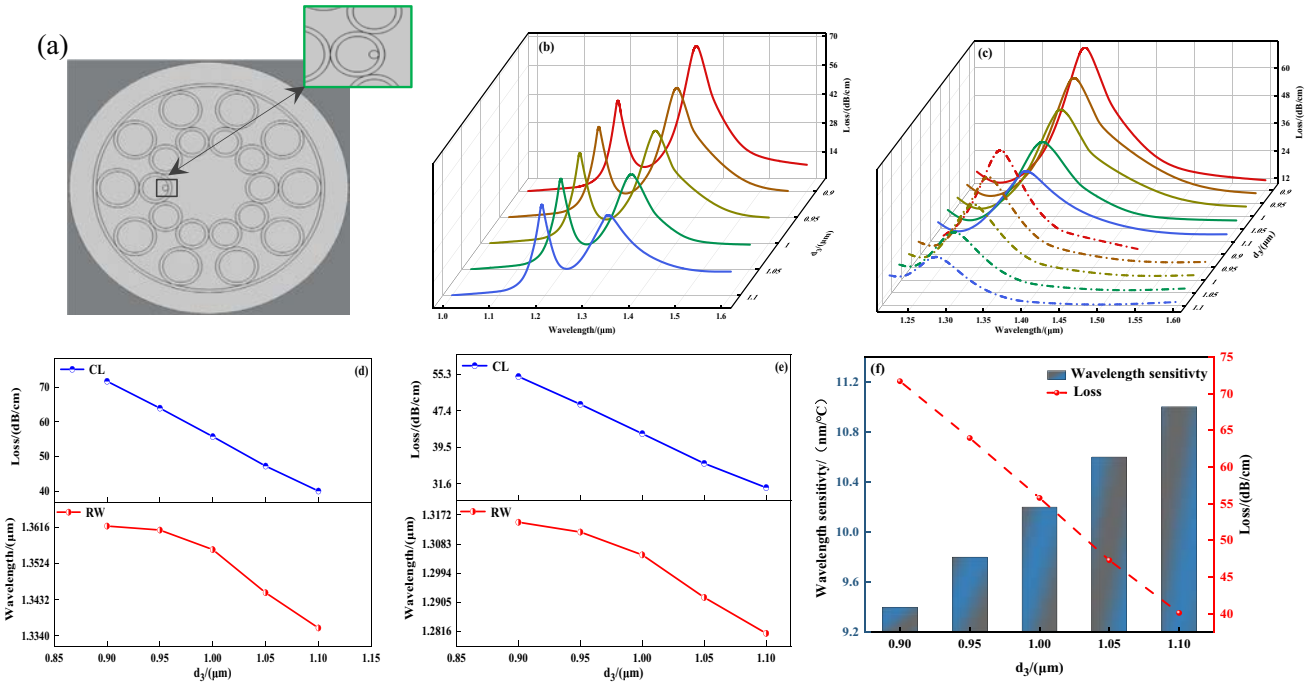

Fig. 5 **a–c** Loss spectra of the ARF-SPR sensor with different gold nanowire diameters. Losses and resonance wavelengths: **d** first and **e** second resonance peaks. **f** Wavelength sensitivity of the second resonance peaks at 20 °C

changes d_1. Therefore, based on the optimized gold nanowire d_3, the sensing properties are analyzed when the distance Λ from the central air hole to the center of the inner tube increases from 9 to 9.8 μm with a 0.2 μm step at 50 Oe and 70 Oe magnetic fields. The optimized inner tube acts as a major contributor to the magnetic field because the central air hole is filled with a magnetic fluid. As the inner tube Λ increases, the second resonance peak resonance wavelength does not shift, and the first resonance peak redshifts. At Λ = 9 μm, the first resonance peak loss is the largest corresponding to a wavelength sensitivity of up to 250 pm/Oe. A decrease in the distance Λ from the central air hole to the center of the inner tube increases the percentage of SiO_2 in the fiber core, thus allowing more energy to be confined within the core and better resonance. Therefore, Λ is chosen to be 9 μm. The diameter of the outer tube is adjusted by varying d_2 around the initial value. Numerical simulation reveals that the magnitude of d_2 has almost no effect on the properties of the sensor and the resonance wavelength does not change. Therefore, the initial value of 6 μm is used for d_2.

The tube wall thickness t is optimized based on the optimized gold nanowires d_3 and inner tube d_1. As shown in Fig. 7b, the resonance wavelength (RW) of the ARF-SPR sensor varies significantly with the thickness of the tube wall. The RW of both resonance peaks shifts to longer wavelengths when the tube wall thickness t is increased from 0.4 to 0.6 μm. This phenomenon can be interpreted as an increase in the real part of the effective refractive index (Re(n_{eff})) of the SPP mode, but there is no significant change in the Re(n_{eff}) of the fundamental mode, and so the phase-matching point (resonance wavelength) of the SPP and fundamental modes moves to a longer wavelength. In addition, the first resonance peak RW changes more significantly, indicating that the tube wall thickness t has a greater influence on the magnetic field. Figure 7c–e show the tube wall thickness t versus resonance wavelength and losses at 50 Oe and 70 Oe magnetic fields. The resonance wavelength curves show large slopes, suggesting that the tube wall thickness affects the refractive index difference between the cladding and the core, thus changing the mode-coupled band. Figure 7f portrays the wavelength sensitivity for different tube wall thicknesses at a magnetic field of 50 Oe, at $t = 0.6$ μm. The first resonance peak confinement loss (CL) is the largest and the wavelength sensitivity is 250 pm/Oe indicating that there is strong coupling between the fundamental and SPP mode to excite SPR, and the two resonance peaks are far away for temperature and magnetic field detection. As a result, $t = 0.6$ μm is selected.

The optimized ARF can be produced by the stacked and quadratic map methods [37, 38]. The liquid gold, temperature-sensitive liquids, and magnetic fluids are pushed into the negative curvature tube by high-pressure chemical vapor deposition (HPCVD) [39]. Several selective filling techniques have been reported to fabricate ARF-SPR sensors for two-parameter detection [40–42].

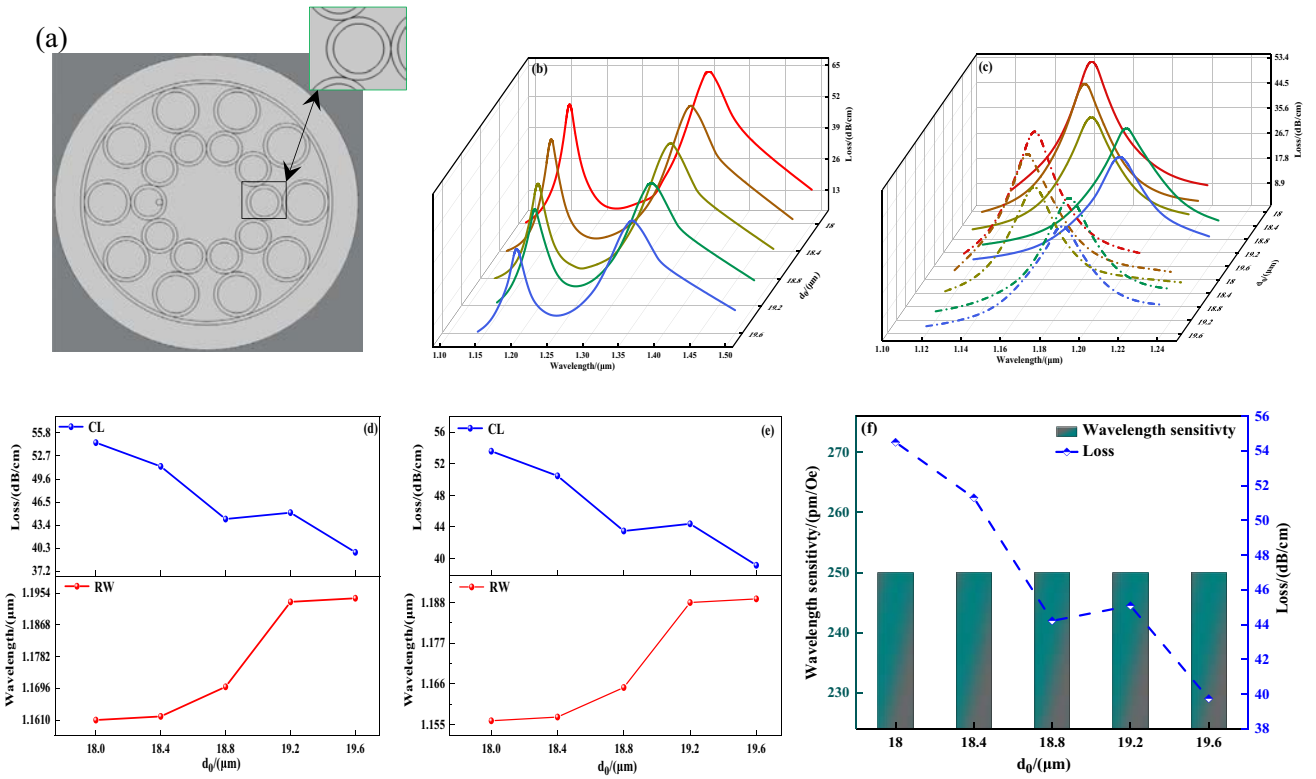

Fig. 6 **a–c** Loss spectra of the ARF-SPR sensors with different inner tube diameters. Losses and resonance wavelengths: **d** first and **e** second resonance peaks. **f** Wavelength sensitivity of the first resonance peak at the 50 Oe magnetic field

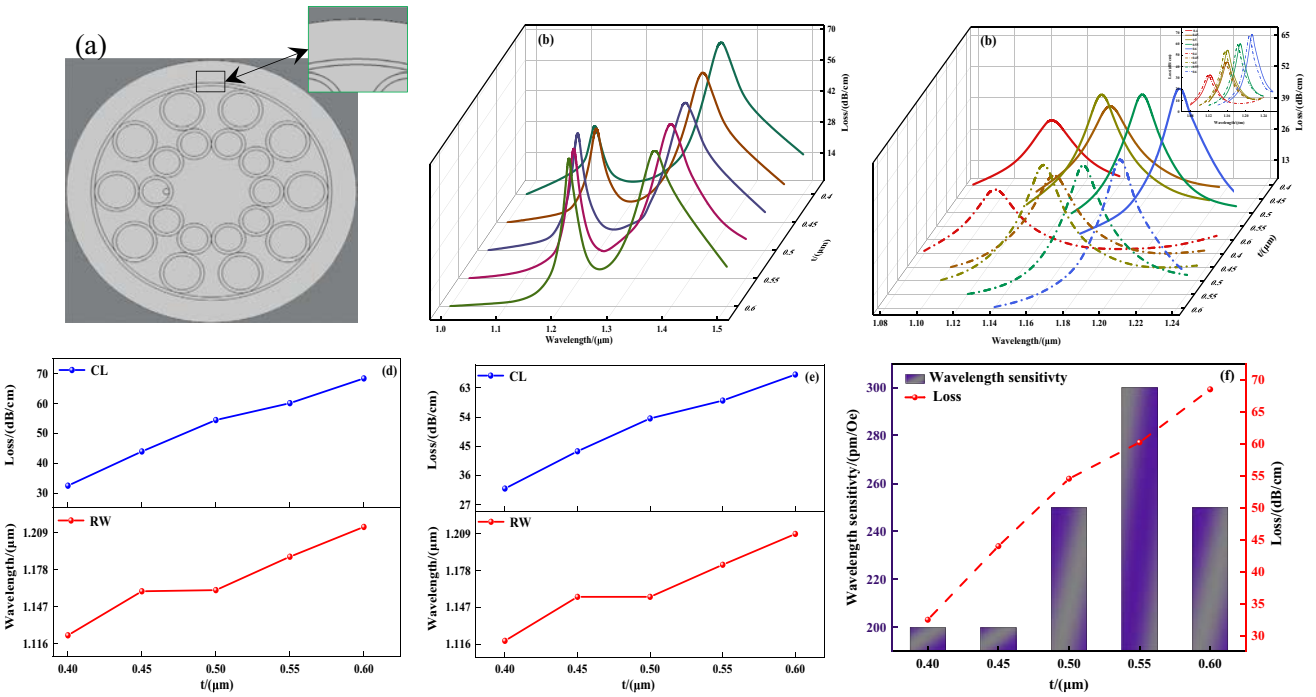

Fig. 7 **a–c** Loss spectra of the ARF-SPR sensors for different tube wall thicknesses. Losses and resonance wavelengths: **d** first and **e** second resonance peaks. **f** Wavelength sensitivity of the first resonance peak at a magnetic field of 50 Oe

The detection process for magnetic field is illustrated in Fig. 8. A broadband light source and optical spectrum analyzer (OSA) are connected to the left and right sides of the SMF, in which the ARF-SPR sensors are embedded to generate different magnetic field strengths and temperatures via the magnetic field and temperature control devices. In the case of magnetic fields, for example, when a broad spectrum of light with wavelengths of 1000–1600 nm is incident in an ARF-SPR sensor, the sensor probe generates SPRs, leading to the formation of resonance valleys in the transmission spectrum. The sensing probe passes through a solenoid coil that can be programmed with a programmable power supply to adjust the current and thus change the strength of the magnetic field. In order to monitor the magnetic field strength in real time, a Gaussmeter was used as a measuring instrument to measure the magnetic field strength around the probe. Different magnetic fields cause the refractive index (RI) of the MF filling the sensor probe to change, thus affecting the transmission of light through the fiber. Finally, the resonance wavelengths of the corresponding loss spectra are acquired by connecting the optical spectrum analyzer (OSA) to the personal computer (PC) for magnetic field.

Results and Discussion

The sensing characteristics including the fitted curves, resolution, structural parameter sensitivity, and figure of merit of the optimized sensor are analyzed using COMSOL for magnetic fields from 50–130 Oe and temperature from 20 to 30 °C.

Magnetic Field and Temperature Sensing

The wavelength sensitivity, which is defined as the ratio of the resonant wavelength shift of the adjacent magnetic field strength or temperature to the adjacent magnetic field strength or temperature change, is one of the most important parameters for the ARF-SPR sensor [21]. Figure 9a displays the curves of resonance wavelength versus loss for different magnetic field strengths. As the magnetic field increases, both resonance peaks blueshift, with the first resonance peak resonant wavelength (RW) changing from 1214 to 1195 nm and the second one from 1370 to 1338 nm. Figure 9b and c summarize the wavelength sensitivity (WS) and confinement loss (CL) of the first and second resonance peaks and Fig. 9a shows magnetic field strengths in the range of 50–130 Oe. The wavelength sensitivity of the second resonance peak is higher than that of the first resonance peak in general. The maximum wavelength sensitivities and average wavelength sensitivities of the first and second resonance peaks are 300 pm/Oe / 500 pm/Oe and 237.5 pm/Oe / 400 pm/Oe, respectively. To analyze the sensitivity of the magnetic field, linear fitting is performed on *RW* of the two resonance peaks and the fitted expressions are:

$$\lambda_1 = 1.2256 - 2.4 \times 10^{-4} H \quad \text{and} \tag{12}$$

$$\lambda_2 = 1.3886 - 4 \times 10^{-4} H \ , \tag{13}$$

where λ_1 and λ_2 are the resonance wavelengths of the first and second resonance peaks, respectively, and H is the magnetic field strength. As shown in Fig. 9d and e, the R^2 values of the first and second resonance peaks are

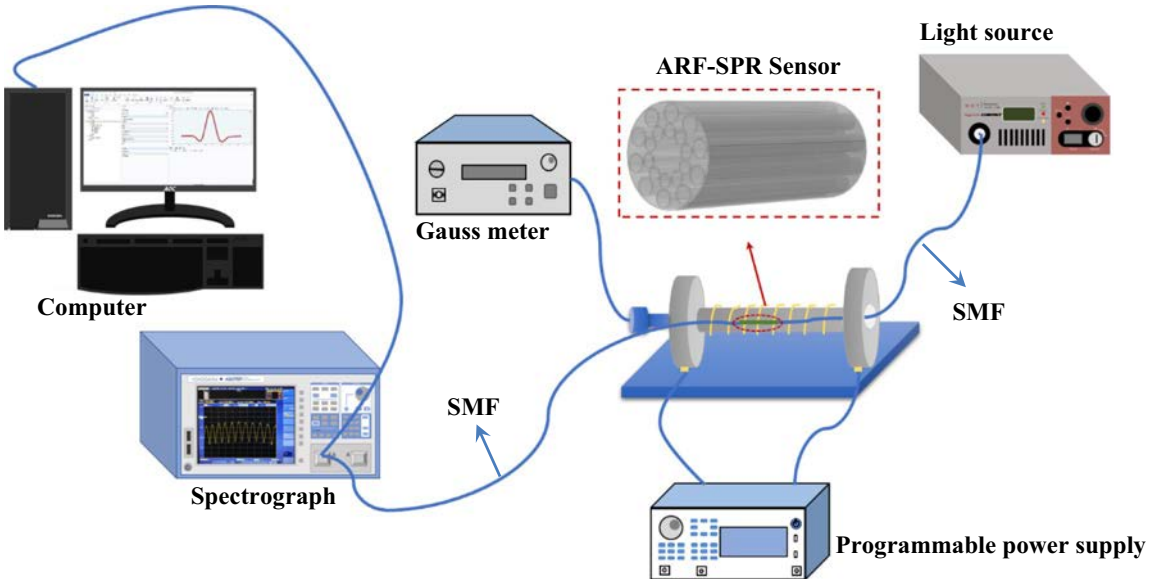

Fig. 8 Schematic diagram of the experimental setup for magnetic field and temperature detection

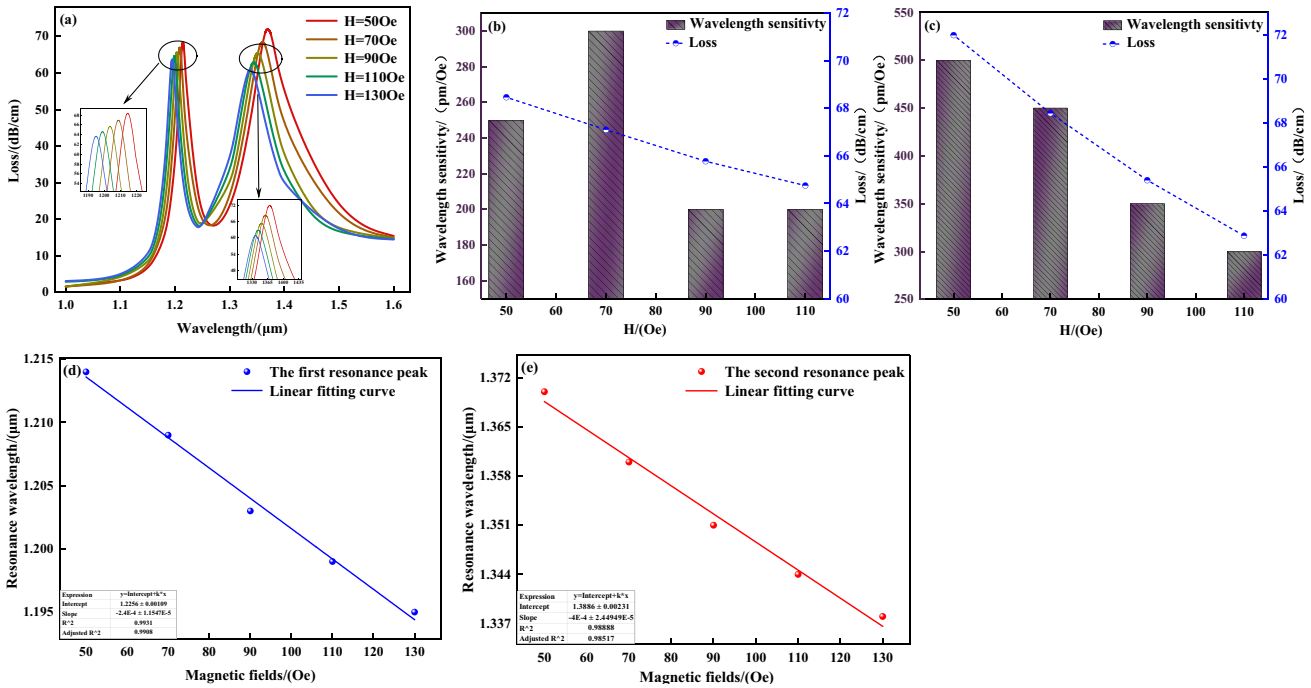

Fig. 9 **a** Loss spectra of the fundamental mode at $H = 50$–130 Oe. **b**, **c** Resonance wavelengths and losses at different magnetic fields. **d**, **e** Linear fits of the first and second resonance peaks

99.31% and 98.89%, respectively, indicating that the sensing characteristics are excellent and the second resonance peak is better than the first resonance peak for magnetic field detection.

The temperature effects on the ARF-SPR sensor are studied. Figure 10a presents the relationship between the resonance wavelength and losses in the temperature range of 20–30 °C. The first resonance peak wavelength sensitivity (RW) does not change, suggesting that the first resonance peak is not sensitive to temperature. The confinement loss (CL) of the second resonance peak decreases gradually as the resonance wavelength blueshifts because the refractive indexes of MF and PDMS decrease with increasing temperature. The effective refractive indexes of the two SPP modes decrease and resonance weakens gradually. It can be verified by Fig. 10b showing that the maximum wavelength sensitivity and average wavelength sensitivity of the second resonance peak are 10.8 nm/°C and 10.6 nm/°C, respectively. The first resonance peak is almost independent of temperature and the temperature sensitivity of the first resonance peak is 0 nm/°C. The temperature versus resonance wavelength relationship can be fitted by Eq. (14) as shown in Fig. 12c [43]:

$$\lambda_2 = 1.581 - 1.056 \times 10^{-2} T \,, \tag{14}$$

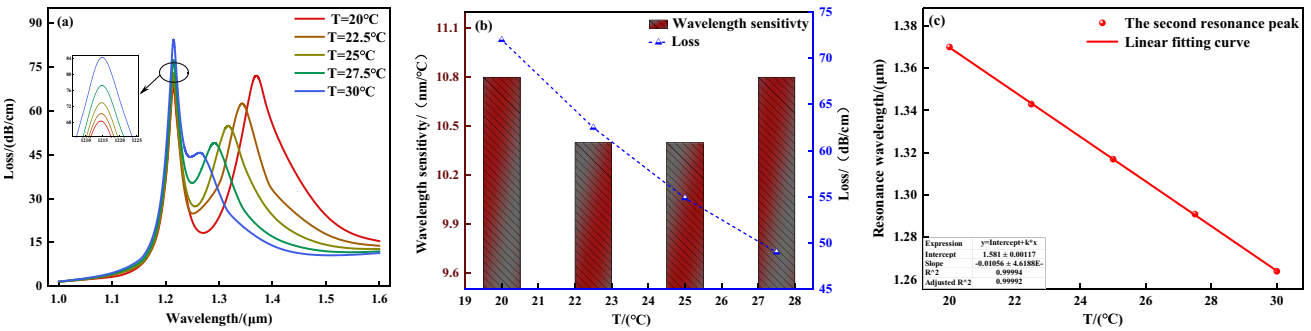

Fig. 10 **a** Loss spectra of the fundamental mode at $T = 20$–30 °C. **b** Resonance wavelengths and losses at different temperatures. **c** Empirical fit of the second resonance peaks

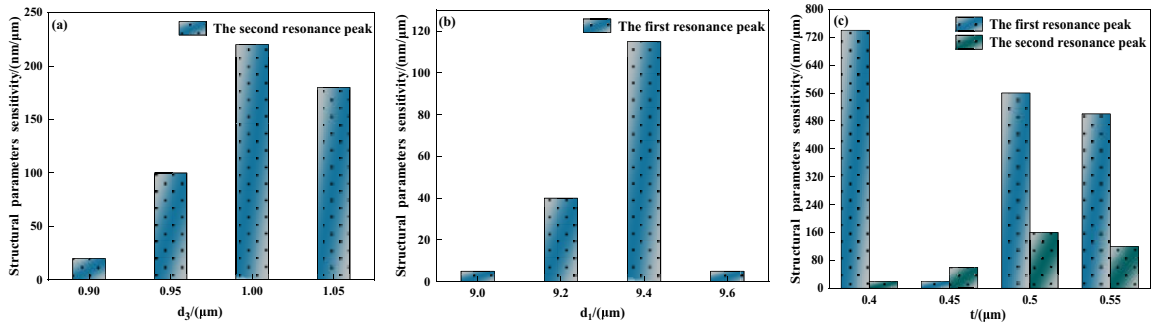

Fig. 11 Sensitivity of structural parameters. **a** Gold nanowire diameter, **b** inner tube diameter, and **c** inner tube inner diameter negative curvature tube thickness

where λ_2 is the resonance wavelength of the second resonance peak and T is the temperature. The R^2 value of the second resonance peak is 99.994%.

Multiparameter sensing based on matrix demodulation enables decoupling of the magnetic field and temperature, thus overcoming the temperature cross-sensitivity issue. The derived magnetic field and temperature sensitivities are solved by Eq. (11) to obtain:

$$\begin{pmatrix} \Delta H \\ \Delta T \end{pmatrix} = \begin{pmatrix} 0.3 & 0 \\ 0.5 & 10.8 \end{pmatrix}^{-1} \begin{pmatrix} \Delta\lambda_1 \\ \Delta\lambda_2 \end{pmatrix}. \tag{15}$$

The other important parameter is the resolution which refers to the ability to detect the smallest change in a weak signal. The lower the resolution, the more sensitive the sensor is to the input signal and the easier the detection. According to Eq. (16) [44]:

$$R_n = \frac{\Delta n_a \Delta\lambda_{\min}}{\Delta\lambda_{peak}} = \frac{\Delta\lambda_{\min}}{S_n}, \tag{16}$$

where S_n is the wavelength sensitivity and $\Delta\lambda_{\min}$ is the minimum measured value of the spectrum analyzer (OSA) usually associated with the instrument. With regard to the magnetic field, the minimum and average resolutions of the first and second resonance peaks are 0.33 Oe / 0.2 Oe and 0.42 Oe / 0.25 Oe, respectively. As for the temperature, the second resonance peak shows a minimum resolution of 0.0096 °C and average resolution of 0.0094 °C. Regarding the temperature and magnetic field, the second resonance peak shows a lower resolution than the first resonance peak due to the higher wavelength sensitivity of the second resonance peak. Hence, its ability to detect weak signals is better than that of the first resonance peak.

Sensitivity of Structural Parameters

The structural parameter sensitivity, defined as the ratio of the resonance wavelength shift to the structural parameter change, is adopted to evaluate the stability of the SPR sensor during manufacturing [45]. Owing to real and objective conditions, the actual characteristics may deviate from theoretical ones due to small changes in the fiber during manufacturing. The sensitivity curves of the structural parameters for the gold nanowires (d_3), inner tube diameter (d_1), and tube wall thickness (t) are plotted in Fig. 11a–c. With regard to the gold nanowire (d_3), the structural parameter sensitivity of the second resonance peak decreases to 20 nm/μm, and for the inner tube diameter (d_1), the sensitivity of the first resonance peak is as small as 5 nm/μm. The thickness of the tube wall affects the sensor, and as shown in the figures,

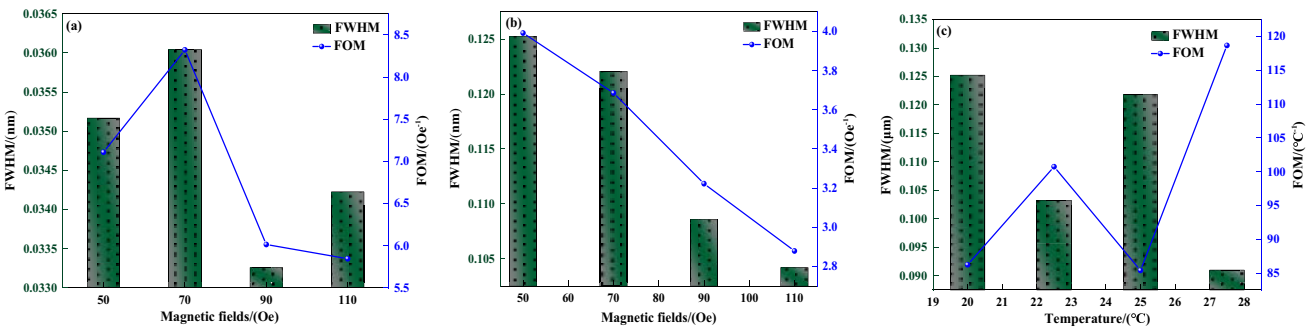

Fig. 12 FOM: **a** magnetic field first resonance peak, **b** magnetic field second resonance peak, and **c** temperature second resonance peak

Table 1 Performance comparison with recently reported sensors

Reference	Fiber type	Material	Detection range	Sensitivity
[11]	PCF	MF	100–160 Oe	5000 pm/Oe
[13]	PCF	Fe_3O_4	100–160 Oe	83,268.46 nm/RIU
[16]	NC-HCF	MF	100–400 Oe	6.8 nm/Oe
[18]	MOF	C_2H_5OH	50–200 Oe, 10–60 °C	25,641 nm/RIU, 10 nm/°C
[20]	PCF	Water	30—70 °C	818 pm/°C
Ours	ARF	MF	50–130 Oe, 20–30 °C	500 pm/Oe, 10.8 nm/°C

the structural sensitivity of both resonance peaks is larger for the thickness of the tube wall (t). The average structural sensitivities of the two peaks are 455 nm/μm and 90 nm/μm, respectively, and consequently, the pipe wall thickness should be precisely controlled during actual manufacturing.

Figure of Merit (FOM)

The figure of merit (FOM) defined as the ratio of wavelength sensitivity to the full-width at half-maximum (FWHM) is derived to evaluate the overall performance of the ARF-SPR sensor. A larger FOM indicates more desirable properties as shown in Eq. (16) [46]:

$$FOM = \frac{S_n}{FWHM} \tag{16}$$

where S_n is the wavelength sensitivity and FWHM refers to the frequency band corresponding to half the height of the confinement loss (CL) peak. Figure 12a and b show the FOM and FWHM values of the first resonance peak and second resonance peak for different magnetic field strengths, and Fig. 12c shows the results of the second resonance peak at different temperatures.

Table 1 compares the optical properties of recently studied magnetic field sensors and temperature sensors. The selection of the filler material and the structure of the fiber have a great influence on the performance of the sensor. The table lists a range of sensors in different materials and configurations. The sensor has a simpler structure than previously proposed sensors and can detect magnetic field and temperature with higher sensitivity over a wider band.

Conclusion

A novel ARF-SPR sensor incorporating MF and PDMS is designed for simultaneous detection of the magnetic field and temperature while avoiding the problem of temperature cross-sensing. By analyzing the effects of the structural parameters of the ARF, the optimal fiber structure size is determined. The modal characteristics of the sensor are investigated by COMSOL. The x-pol mode has better sensing characteristics. In the magnetic field range of 50–130 Oe and temperature range of 20–30 °C, the magnetic field and temperature resolutions are below 0.5 Oe and 0.0096 °C, respectively, with a minimum structural sensitivity of 5 nm/μm and maximum FOM of 118.681 $°C-^{1}$. Compared with other magnetic field sensors, this ARF-SPR sensor boasting a simple structure, high sensitivity, and easy manufacturing has great potential in aerospace applications, long-distance transmission, and complex environmental monitoring.

Author Contribution ML, XL, and CL made substantial contributions to the conception or design of the work; the acquisition, analysis, or interpretation of data; and the creation of new software used in the work. WL, XL, and JL drafted the work or revised it critically for important intellectual content. KX approved the version to be published. LY, JW, and PKC agree to be accountable for all aspects of the work in ensuring that questions related to the accuracy or integrity of any part of the work are appropriately investigated and resolved.

Funding This work was jointly supported by the Heilongjiang Provincial Natural Science Foundation of China [JQ2023F001], Local Universities Reformation and Development Personnel Training Supporting Project from Central Authorities, Outstanding young and middle-aged research and innovation team of Northeast Petroleum University [KYCXTD201801], Postdoctoral scientific research development fund of Heilongjiang Province (LBH-Q20081), City University of Hong Kong Donation Research Grants [DON-RMG Nos. 9229021 and 9220061], and City University of Hong Kong Strategic Research Grant [SRG 7005505].

Availability of Data and Material Not applicable.

Code Availability Not applicable.

Declarations

Ethics Approval and Consent to Participate Approved.

Consent for Publication Approved.

Competing Interests The authors declare no competing interests.

References

1. Zhou X, Li X, Li S et al (2018) Magnetic field sensing based on SPR optical fiber sensor interacting with magnetic fluid. IEEE

Trans Instrum Meas 68(1):234–239. https://doi.org/10.1109/TIM.2018.2834222
2. Liu C, Shen T, Wu HB et al (2021) Applications of magneto-strictive, magneto-optical, magnetic fluid materials in optical fiber current sensors and optical fiber magnetic field sensors: A review. Opt Fiber Technol 65:102634. https://doi.org/10.1016/j.yofte.2021.102634
3. Kamkar A, Ahmed K, Alam MS et al (2021) SPR sensor-based sensitivity performance investigation using an H-shaped model with supportive metal variation. Plasmonics 16(4):1327–1337. https://doi.org/10.1007/s11468-021-01391-z
4. Li W, Wang J (2014) Magnetic sensors for navigation applications: an overview. The Journal of navigation 67(2):263–275. https://doi.org/10.1017/S0373463313000544
5. Pappas DP (2008) High sensitivity magnetic field sensor technology overview. National Institute of Standards & Technology Boulder, CO
6. Alberto N, Domingues MF, Marques C et al (2018) Optical fiber magnetic field sensors based on magnetic fluid: a review. Sensors 18(12):4325. https://doi.org/10.3390/s18124325
7. Yang M, Dai J, Zhou C et al (2009) Optical fiber magnetic field sensors with TbDyFe magnetostrictive thin films as sensing materials. Opt Express 17(23):20777–20782. https://doi.org/10.1364/OE.17.020777
8. Paliwal A, Tomar M, Gupta V (2018) Study of optical properties of Ce and Mn doped BiFeO3 thin films using SPR technique for magnetic field sensing. Vacuum 158:48–51. https://doi.org/10.1016/j.vacuum.2018.09.018
9. Mitu SA, Ahmed K, Bui FM (2023) Magnetic biosensors. Biosensors Nanotechnology 201–213. https://doi.org/10.1002/9781394167135.ch10
10. Chen Y, Han Q, Liu T et al (2013) Optical fiber magnetic field sensor based on single-mode–multimode–single-mode structure and magnetic fluid. Opt Lett 38(20):3999–4001. https://doi.org/10.1364/OL.38.003999
11. Mitu SA, Ahmed K, Hossain MN et al (2020) Design of magnetic fluid sensor using elliptically hole assisted photonic crystal fiber (PCF). J Supercond Novel Magn 33:2189–2198. https://doi.org/10.1007/s10948-020-05476-4
12. Agruzov PM, Pleshakov IV, Bibik EE et al (2014) Magneto-optic effects in silica core microstructured fibers with a ferrofluidic cladding. Appl Phys Lett 104(7). https://doi.org/10.1063/1.4866165
13. Mitu SA, Dey DK, Ahmed K et al (2020) Fe3O4 nanofluid injected photonic crystal fiber for magnetic field sensing applications. J Magn Magn Mater 494:165831. https://doi.org/10.1016/j.jmmm.2019.165831
14. Zhao Y, Lv RQ, Wang D et al (2014) Fiber optic Fabry-Perot magnetic field sensor with temperature compensation using a fiber Bragg grating. IEEE Trans Instrum Meas 63(9):2210–2214. https://doi.org/10.1109/TIM.2014.2308360
15. Luo L, Pu S, Dong S et al (2015) Fiber-optic magnetic field sensor using magnetic fluid as the cladding. Sens Actuators, A 236:67–72. https://doi.org/10.1016/j.sna.2015.10.034
16. Mitu SA, Ahmed K, Bui FM et al (2021) Novel nested anti-resonant fiber based magnetic fluids sensor: performance and bending effects inspection. J Magn Magn Mater 538:168230. https://doi.org/10.1016/j.jmmm.2021.168230
17. Liu H, Li H, Wang Q et al (2018) Temperature-compensated magnetic field sensor based on surface plasmon resonance and directional resonance coupling in a D-shaped photonic crystal fiber. Optik 158:1402–1409. https://doi.org/10.1016/j.ijleo.2018.01.033
18. Abdullah H, Mitu SA, Ahmed K (2020) Magnetic fluid-injected ring-core-based micro-structured optical fiber for temperature sensing in broad wavelength spectrum. J Electron Mater 49:4969–4976. https://doi.org/10.1007/s11664-020-08231-6
19. Wang D, Yi Z, Ma G et al (2022) Two-channel photonic crystal fiber based on surface plasmon resonance for magnetic field and temperature dual-parameter sensing. Phys Chem Chem Phys 24(35):21233–21241. https://doi.org/10.1039/D2CP02778J
20. Alam MS, Akter S, Paul BK et al (2019) FEM based highly sensitive dual core temperature sensor: design and analysis. OSA Continuum 2(9):2581–2592. https://doi.org/10.1364/OSAC.2.002581
21. Liu W, Shi Y, Yi Z et al (2021) Surface plasmon resonance chemical sensor composed of a microstructured optical fiber for the detection of an ultra-wide refractive index range and gas-liquid pollutants. Opt Express 29(25):40734–40747. https://doi.org/10.1364/OE.444323
22. Wang S, Gao J (2023) Overview of magnetic field sensor[C]//Journal of Physics: Conference Series. IOP Publishing 2613(1):012012. https://doi.org/10.1088/1742-6596/2613/1/012012
23. Gao H, Hu H, Zhao Y et al (2018) Highly-sensitive optical fiber temperature sensors based on PDMS/silica hybrid fiber structures. Sens Actuators, A 284:22–27. https://doi.org/10.1016/j.sna.2018.10.011
24. Kumar S, Malik MM, Purohit R (2017) Synthesis methods of mesoporous silica materials. Materials Today: Proceedings 4(2):350–357. https://doi.org/10.1016/j.matpr.2017.01.032
25. Sun G, Liu Q, Mu H et al (2023) Anti-resonant fiber with nested U-shape tubes for low-loss terahertz waveguides. Opt Laser Technol 163:109424. https://doi.org/10.1016/j.optlastec.2023.109424
26. Liu Q, Sun G, Mu H et al (2024) Hybrid nested negative curvature fiber with ultra-low-loss in the terahertz band. Infrared Phys Technol 136:105003. https://doi.org/10.1016/j.infrared.2023.105003
27. Zhu Y, Cheng J, Yi Z et al (2023) Spectrally selective solar absorber and thermal infrared suppression based on hollow cylindrical microstructures. Optics Communications 549:129910. https://doi.org/10.1016/j.optcom.2023.129910
28. Liu M, Leng X, Ni W et al (2023) Ultrahigh sensitivity refractive index sensor based on surface plasmon resonance effect of double-ring hollow-core anti-resonant fiber. Plasmonics 1–11
29. Liu Y, Bo M, Yang X et al (2017) Size modulation electronic and optical properties of phosphorene nanoribbons: DFT–BOLS approximation. Phys Chem Chem Phys 19(7):5304–5309. https://doi.org/10.1039/C6CP08011A
30. Budker D, Romalis M (2007) Optical magnetometry. Nat Phys 3(4):227–234
31. Li Y, Chen H, Chen Q et al (2023) Surface plasmon resonance induced methane gas sensor in hollow core anti-resonant fiber. Opt Fiber Technol 78:103293. https://doi.org/10.1016/j.yofte.2023.103293
32. He L, Yi Y, Zhang J et al (2024) A four-narrowband terahertz tunable absorber with perfect absorption and high sensitivity. Mater Res Bull 170:112572. https://doi.org/10.1016/j.materresbull.2023.112572
33. Sharma AK, Jha R, Gupta BD (2007) Fiber-optic sensors based on surface plasmon resonance: a comprehensive review. IEEE Sens J 7(8):1118–1129. https://doi.org/10.1109/JSEN.2007.897946
34. Lu W, Yi Z, Zhang J et al (2023) A tunable broadband absorber in the terahertz band based on the proportional structure of a single layer of graphene. Diam Relat Mater 140:110481. https://doi.org/10.1016/j.diamond.2023.110481
35. Mumtaz F, Roman M, Zhang B et al (2022) A simple optical fiber SPR sensor with ultra-high sensitivity for dual-parameter measurement. IEEE Photonics J 14(5):1–7. https://doi.org/10.1109/JPHOT.2022.3203930
36. Liu C, Yang L, Liu Q et al (2018) Analysis of a surface plasmon resonance probe based on photonic crystal fibers for low refractive index detection. Plasmonics 13:779–784
37. Nawazuddin MBS, Wheeler NV, Hayes JR et al (2017) Lotus-shaped negative curvature hollow core fiber with 10.5 dB/km at 1550 nm wavelength. J Light Technol 36(5):1213–1219. https://doi.org/10.1109/JLT.2017.2787197

38. Warren-Smith SC, Ebendorff-Heidepriem H, Foo TC et al (2009) Exposed-core microstructured optical fibers for real-time fluorescence sensing. Opt Express 17(21):18533–18542. https://doi.org/10.1364/OE.17.018533
39. Sazio PJA, Amezcua-Correa A, Finlayson CE et al (2006) Microstructured optical fibers as high-pressure microfluidic reactors. Science 311(5767):1583–1586. https://doi.org/10.1126/science.1124281
40. Kuhlmey BT, Eggleton BJ, Wu DKC (2009) Fluid-filled solid-core photonic bandgap fibers. J Lightwave Technol 27(11):1617–1630. https://doi.org/10.1109/JLT.2009.2021142
41. Wang Y, Liao CR, Wang DN (2010) Femtosecond laser-assisted selective infiltration of microstructured optical fibers. Opt Express 18(17):18056–18060. https://doi.org/10.1364/OE.18.018056
42. Vieweg M, Gissibl T, Pricking S et al (2010) Ultrafast nonlinear optofluidics in selectively liquid-filled photonic crystal fibers. Opt Express 18(24):25232–25240. https://doi.org/10.1364/OE.18.025232
43. Liu T, Liu Y, Ling L et al (2023) Multifunctional terahertz device with active switching between bimodal perfect absorption and plasmon-induced transparency. Mater Res Bull 112635. https://doi.org/10.1016/j.materresbull.2023.112635
44. Jorgenson RC, Yee SS (1993) A fiber-optic chemical sensor based on surface plasmon resonance. Sens Actuators, B Chem 12(3):213–220. https://doi.org/10.1016/0925-4005(93)80021-3
45. Gupta BD, Sharma AK (2005) Sensitivity evaluation of a multi-layered surface plasmon resonance-based fiber optic sensor: a theoretical study. Sens Actuators, B Chem 107(1):40–46. https://doi.org/10.1016/j.snb.2004.08.030
46. Abdelghani A, Chovelon JM, Jaffrezic-Renault N et al (1997) Surface plasmon resonance fibre-optic sensor for gas detection. Sens Actuators, B Chem 39(1–3):407–410. https://doi.org/10.1016/S0925-4005(97)80243-2